HHS Public Access

Author manuscript

Science. Author manuscript; available in PMC 2019 December 27.

Published in final edited form as:

Science. 2019 October 18; 366(6463): 360–364. doi:10.1126/science.aax1562.

Rapid, large-volume, thermally controlled 3D printing using a mobile liquid interface

David A. Walker[1,2,*], **James L. Hedrick**[2,3,*], **Chad A. Mirkin**[1,2,3,†]

[1]Department of Chemistry, Northwestern University, Evanston, IL 60208, USA.

[2]International Institute for Nanotechnology, Northwestern University, Evanston, IL 60208, USA.

[3]Department of Chemical and Biological Engineering, Northwestern University, Evanston, IL 60208, USA.

Abstract

We report a stereolithographic three-dimensional printing approach for polymeric components that uses a mobile liquid interface (a fluorinated oil) to reduce the adhesive forces between the interface and the printed object, thereby allowing for a continuous and rapid print process, regardless of polymeric precursor. The bed area is not size-restricted by thermal limitations because the flowing oil enables direct cooling across the entire print area. Continuous vertical print rates exceeding 430 millimeters per hour with a volumetric throughput of 100 liters per hour have been demonstrated, and proof-of-concept structures made from hard plastics, ceramic precursors, and elastomers have been printed.

Additive manufacturing has been a disruptive force (1–7). Traditionally, it has been used for prototyping, substantially reducing the time from product ideation to manufacturing, but it has recently begun to make notable progress in the manufacturing sector (8, 9). One promising approach for the printing of plastic objects is stereo-lithography (SLA), which uses photocurable liquid resins that can be chemically formulated to yield materials with a large range of attractive mechanical properties (10, 11). Conventional SLA operates by using ultraviolet (UV) light to cure liquid photoactive resins on a vertically moving plate; the result is a desired three-dimensional (3D) object consisting of stacked 2D layers (12). DeSimone and co-workers introduced a variation of SLA called continuous liquid interface printing, which uses oxygen inhibition to create a reaction “dead layer” (13, 14). This dead layer pre-vents adhesion between the emerging part and the bottom of the print vat, obviating the need to repeatedly mechanically cleave the part from the vat (12). This

† Corresponding author. chadnano@northwestern.edu.

Author contributions: All authors contributed to the ideas explored in this manuscript, data analysis, and writing and editing of the manuscript. D.A.W. and J.L.H. performed experiments. C.A.M. directed the work.

*These authors contributed equally to this work.

Competing interests: The authors have financial interests in Azul 3D Inc., a company that has licensed the HARP intellectual property (U.S. Patent Application 62/815,175). D.A.W., J.L.H., and C.A.M. all have secondary affiliations with Azul 3D Inc.

Data and materials availability: All data are available in the main text or the supplementary materials. Butadiene rubber and ABS-like urethane acrylate resins require a material transfer agreement to be sampled.

SUPPLEMENTARY MATERIALS

science.sciencemag.org/content/366/6463/360/suppl/DC1

continuous print approach increases vertical print speeds by two orders of magnitude while simultaneously removing material defects intrinsic to the aforementioned layer-by-layer lamination approaches. However, the polymerization re-actions used in SLA photoresins are highly exothermic, and at such print speeds, the challenge of heat dissipation is daunting (15, 16). Moreover, the delivery of gaseous oxygen, a thermal insulator, through the print bed to create a dead layer limits one to peripheral cooling options that cannot rapidly dissipate the heat being generated.

We report a dead layer–free approach to rapid SLA printing, HARP (high-area rapid printing), which is capable of continuously printing over large areas and at rapid vertical print speeds. The printer operates on the principle of a UV-curable resin floating on a bed of flowing immiscible fluorinated oil to minimize interfacial adhesion at the build region. Aizenberg and co-workers have demonstrated the great breadth of dewetting behavior possible when using fluorinated liquids embedded within solid matrices for applications in medicine and marine biofouling (17, 18). HARP builds on this concept by keeping the fluorinated phase in constant motion relative to the emerging printed part, further decreasing the adhesion forces (i.e., static versus dynamic) and generating a solid-liquid slip boundary. The oil can be recirculated through a heat exchanger to cool or heat the build region and maintain thermostatic control across the entire print bed. Additionally, the oil can be continuously filtered to remove the microparticulate solids that are generated during the SLA print process and decrease resolution through light scattering (commonly referred to as “clouding”) (19). Finally, because HARP does not require an oxygen dead layer, it is compatible with both oxygen-sensitive and -insensitive ink chemistries, increasing the scope of applicable resins and resulting materials.

HARP operates through a mobile liquid interface that creates a shear stress beneath the emerging part and results in a slip boundary (Fig. 1). The slip boundary allows for the solidified part to be continuously retracted from the print interface. Fluorinated oils (perfluoro-polyether copolymers, such as Solvay Fomblin Y or Chemours Krytox GPL) were chosen for their omniphobic properties and higher densities relative to that of common SLA resins. Although we explored other immiscible liquid systems, including densified water and glycerin, neither of these aqueous options produced the same quality of dewetting behavior with the emerging 3D printed part; both resulted in lower-quality print production (see fig. S7). A pair of inlet and outlet manifolds were fabricated to distribute a laminar flow of oil across the print bed with a uniform velocity profile (fig. S1). This flow profile ensures that the oil layer remains optically uniform across the build platform (i.e., no turbulence giving rise to optical distortions at the oil/resin interface) and results in a uniform interfacial-shear stress being applied to all solidified parts.

To confirm our hypothesis of a slip boundary being central to the HARP printer’s operation, we used particle imaging velocimetry to analyze the cross-sectional fluid flow profile as the oil passed beneath a printed part (20). Slip boundary conditions are notoriously difficult to observe because of the randomized optical reflections that occur at the interfaces under study, resulting in noisy data (21, 22). To rectify this problem, we fit an analytical model, allowing for the possibility of either a slip or non-slip boundary condition, to the center of the flow profile (i.e., where high-quality data can be collected). The model allowed for a

classical Navier slip boundary to arise when the interfacial shear stress exceeded a given critical shear stress (23). From this analysis, the slip boundary model best captured the dynamics of the experimental data (Fig. 1B and fig. S3) (24). This is best reflected in the experimental velocity profiles [$v_x(y)$; circles in Fig. 1B] as a function of the oil flow rate (increasing volumetric flux, from red to violet) and the corresponding Navier slip model fits (solid lines in Fig. 1B).

In the absence of heat removal, rapid vertical print speeds of even modestly sized parts quickly exceed the smoke point of the resin. These extreme temperature swings ($\Delta T \approx$ >120°C) result in variable reactivities across the print bed, thermal warping/cracking of the printed material, and uncontrolled clouding that limits lateral resolution; ultimately these factors result in a deformed object and failed print (fig. S6) (24). To quantify the ability of HARP to dissipate heat, we performed thermal imaging of a small test print (5 cm × 5 cm cross-sectional dimensions) in a specially designed miniature print vat (i.e., low-profile walls to enable imaging across the bed). Three different flow scenarios were evaluated: (i) printing without a mobile interface or active cooling (Fig. 2A); (ii) printing with a mobile interface to actively dissipate heat, but with no cooling of the oil (Fig. 2B); and (iii) printing with a mobile interface and active cooling of the oil (Fig. 2C). Without flow to actively dissipate heat, the printed part quickly exceeded the sensor range of the infrared (IR) camera at 150°C, and exceeded the flashpoint of the resin's primary monomer diluent (1,6-hexanediol diacrylate, 113°C). Similar experiments involving the generation of parts having larger cross-sectional areas (e.g., 20 cm × 20 cm) exceeded 180°C (as evidenced by an IR noncontact thermometer gun measurement) in the absence of an active flow to dissipate the accumulating heat. In the case presented here, the accumulation of heat (Fig. 2A) led to surface temperatures in excess of 150°C and the part cracked during the printing process, causing a physical displacement from the stage (observable in the final frame of Fig. 2A, indicated by white lines overlaid on the part; see also fig. S6). Alternatively, the flow of oil depicted in Fig. 2B dissipated this heat into an oil reservoir. Over time, the temperature of the reservoir increased, reducing its effectiveness. Last, in Fig. 2C the oil was actively cooled while flowing to help stabilize the reservoir temperature, as well as the surface temperature of the emerging part, at 100° to 120°C.

To further evaluate the scalability of HARP through cooling, we printed a 38 cm × 61 cm × 76 cm part in 1 hour and 45 min with volumetric throughput of 100 liters/hour (fig. S4). At this scale, the fidelity of the print was affected by the resin's contractility [i.e., the volumetric reduction undergone during the resin solidification process, common to all SLA resins and different for each resin formulation (25)], because even modest contractions of a few percent were amplified into observable bowing. In contrast, when smaller single parts were produced, this contractility became less evident and print fidelity increased (Fig. 3C). Full use of the large-scale capabilities enabled by HARP will require the development of new SLA resins with lower volumetric contractility.

By not relying on oxygen quenching, HARP is capable of printing both oxygen-sensitive and oxygen-insensitive resin chemistries. To demonstrate this ability, we printed three different resins on the HARP 3D printer to generate three different classes of materials with varied properties: a hard polyurethane acrylate, an elastomeric butadiene rubber, and a

silicon carbide ceramic (see Fig. 4). These resins are a mix of resins found in the literature (26, 27), obtained from companies, and formulations developed for the HARP printer. As with all SLA systems, each resin must be optimized in terms of initiators and blockers to perform in conjunction with the light engine used and the desired vertical print rate. This was optimized by altering the photo-initiators used and tuning their concentrations to achieve a desired energy cure and penetration depth response for each resin (24). The hard polyurethane resin printed optimally under a vertical print speed of 120 μm/s. The ceramic resin used thioleneclick chemistry, a chemistry known to be relatively oxygen-insensitive (28, 29), to cross-link the polymeric resin and produce a "green" part. This polymeric silicone can be post-treated in a furnace at 1000°C to undergo pyrolysis to eliminate the organic components and produce a silicon carbide structure (26). Finally, the butadiene rubber resin required a slower print speed (30 μm/s) owing to its lower re-activity and higher viscosity. Although the postprocessing and print conditions differed for each resin (Fig. 4) (24), all the resins were compatible with the HARP approach. This makes HARP printing generally useful with stereolithographic resins currently available through literature or commercial formulations (26, 29).

To determine whether the HARP continuous print process produces isotropic materials, we performed mechanical testing on dog-bone structures printed from an ABS (acrylonitrile butadiene styrene)–like urethane acrylate resin in multiple orientations. This was done using the protocols of ASTM standard D638 for Type I dog bones (30). The results show that the HARP-printed material maintains isotropic mechanical properties comparable to a molded part (Fig. 3A) and that these properties are independent of print orientation, unlike other modes of noncontinuous printing (fig. S8) (24). The HARP parts exhibited mechanical properties comparable to those of injection-molded ABS plastic (Fig. 3A, gray line). In addition, the HARP-printed structures could be made with high print fidelity (Fig. 3, B and C), resolving features as small as 300 μm (the theoretical optical resolution is 100 μm and is a function of the light-patterning engine) and achieving a volumetric correlation of 93% on a test print.

HARP-printed parts have a surface ridging that depends on the minimal wall thickness of the object being printed; thinner part sections result in faster resin replenishment rates and consequently yield a smoother surface. Note that this surface roughness is different from the discrete lamination layers in parts produced by traditional SLA [both digital light processing (DLP) and laser-based approaches] and is independent of the vertical resolution of the slice patterns being sent to the light-patterning engines (10 mm z-height). To further characterize this phenomenon, we printed an array of 80 Type IV dog-bone structures of various thicknesses (1 to 3 mm) and widths (1 to 6 mm) within the necks of the bones at a vertical print rate of 120 μm/s. We then characterized the surfaces via optical microscopy and profilometry to quantify the magnitude of the profiles and the arithmetic surface roughness for each geometry. The maximum roughness, from peak to valley, was determined to be within ±100 μm (i.e., ±1 optical pixel) for all samples (Fig. 3D and fig. S9) (24), with substantially smoother surfaces for parts with a minimal dimension not exceeding 1.5 mm (within ±10 μm). The arithmetic surface roughness strongly correlated with the minimum part dimension (i.e., width or thickness; Fig. 3E) with a Pearson correlation coefficient of $r = 0.90$ ($n = 20$, $r_{crit} = 0.444$ for $P = 0.05$ representing a 95% confidence level). Additionally,

we printed a series of dog-bone structures (80 dog bones, five unique geometries in replicate; 120 μm/s vertical print rate) similar to a Type IV dog bone in profile, but with various thicknesses ranging from 1 to 3 mm (a typical Type IV dog bone is 3.175 mm thick). Although differing geometries can give rise to slight variations in tensile properties, our hypothesis was that despite the varying dog-bone thickness affecting the surface roughness, the bulk material properties would be relatively invariant (Fig. 3F). Indeed, the Pearson correlation coefficient between the surface roughness and maximum tensile stress is $r = -0.34$ (n = 25, $r_{crit} = 0.396$ for $P = 0.05$ representing a 95% confidence level; Fig. 3F, inset), validating this hypothesis.

Taken together, these advances in through-put, mobile interface design, and materials generality solve several problems associated with large-area, large-object 3D printing. Several challenges remain, including the development of high-speed optical systems capable of retaining high lateral resolution and delivering high optical densities through the interface. Additionally, stereolithographic systems, which operate at high vertical speeds, remain limited by the availability of low-viscosity and low-contractility resins, which can be used to generate structures with industrially relevant properties.

Supplementary Material

Refer to Web version on PubMed Central for supplementary material.

ACKNOWLEDGMENTS

We thank M. Flynn and J. Valdillez for their assistance in developing the light-patterning engines and software used to operate the printer, J. Fernandez for his contributions to understanding of the fluidic flow behavior and the CAD design of objects printed on the HARP process, and R. Davis, R. Schmidt, and E. Cottiss for their assistance in designing and analyzing resins for the printer.

Funding: This material is based on work supported by the Air Force Office of Scientific Research under award FA9550-16-1-0150 (to develop the HARP technology, to perform the velocimetry and thermal imaging, and to develop the ceramic resin); the Center for Bio-Inspired Energy Science, an Energy Frontier Research Center funded by the U.S. Department of Energy, Office of Science, Basic Energy Sciences under award DE-SC0000989 (initial UV-curable rigid urethane resin formulation); the Sherman Fairchild Foundation Inc. (initial UV-curable flexible urethane resin formulation); and a National Defense, Science and Engineering Graduate Fellowship (J.L.H.). CT imaging work was performed by A. Brikha at the Northwestern University Center for Advanced Molecular Imaging, supported by NCI CCSG P30 CA060553 awarded to the Robert H. Lurie Comprehensive Cancer Center.

REFERENCES AND NOTES

1. Gross BC, Erkal JL, Lockwood SY, Chen C, Spence DM, Anal. Chem 86, 3240–3253 (2014). [PubMed: 24432804]
2. Huang SH, Liu P, Mokasdar A, Hou L, Int. J. Adv. Manuf. Technol 67, 1191–1203 (2013).
3. Kruth JP, Leu MC, Nakagawa T, CIRP Ann. 47, 525–540 (1998).
4. Petrick IJ, Simpson TW, Res. Technol. Manag 56, 12–16 (2013).
5. Kelly BE. et al., Science 363, 1075–1079 (2019). [PubMed: 30705152]
6. de Beer MP. et al., Sci. Adv. 5, eaau8723 (2019).
7. Truby RL, Lewis JA, Nature 540, 371–378 (2016). [PubMed: 27974748]
8. Ngo TD, Kashani A, Imbalzano G, Nguyen KTQ, Hui D, Composites B 143, 172–196 (2018).
9. Wohlers T, Caffrey T, Manufact. Eng 150, 67–73 (6 2013).
10. Zheng X. et al., Science 344, 1373–1377 (2014). [PubMed: 24948733]
11. Yagci Y, Jockusch S, Turro NJ, Macromolecules 43, 6245–6260 (2010).

12. Bártolo PJ, Stereolithography: Materials, Processes and Applications (Springer, 2011).
13. Tumbleston JR. et al., Science 347, 1349–1352 (2015). [PubMed: 25780246]
14. Janusziewicz R, Tumbleston JR, Quintanilla AL, Mecham SJ, DeSimone JM, Proc. Natl. Acad. Sci. U.S.A 113, 11703–11708 (2016).
15. Narahara H, Tanaka F, Kishinami T, Igarashi S, Saito K, Rapid Prototyp. J 5, 120–128 (1999).
16. Corcione CE, Greco A, Maffezzoli A, Polym. Eng. Sci 46, 493–502 (2006).
17. Wong T-S. et al., Nature 477, 443–447 (2011). [PubMed: 21938066]
18. Amini S. et al., Science 357, 668–673 (2017). [PubMed: 28818939]
19. Unkovskiy A. et al., Dent. Mater 34, e324–e333 (2018). [PubMed: 30293688]
20. Thielicke W, Stamhuis E, Open Res J. Softw. 2, 30–39 (2014).
21. Huang P, Guasto JS, Breuer KS, Fluid Mech J. 566, 447–464 (2006)
22. Tretheway DC, Meinhart CD, Phys. Fluids 14, L9–L12 (2002).
23. Kaoullas G, Georgiou GC, Non-Newt J. Fluid Mech. 197, 24–30 (2013).
24. [See supplementary materials.]
25. Kuang X. et al., Macromol. Rapid Commun 39, e1700809 (2018)
26. Eckel ZC. et al., Science 351, 58–62 (2016). [PubMed: 26721993]
27. Liew L-A. et al., Sens. Actuators A 95, 120–134 (2002).
28. Husár B, Ligon SC, Wutzel H, Hoffmann H, Liska R, Prog. Org. Coat 77, 1789–1798 (2014).
29. Ligon SC, Liska R, Stampfl J, Gurr M, Mülhaupt R, Chem. Rev 117, 10212–10290 (2017).
30. ASTM D638–10, Standard Test Method for Tensile Properties of Plastics (2010); www.astm.org/DATABASE.CART/HISTORICAL/D638-10.htm.

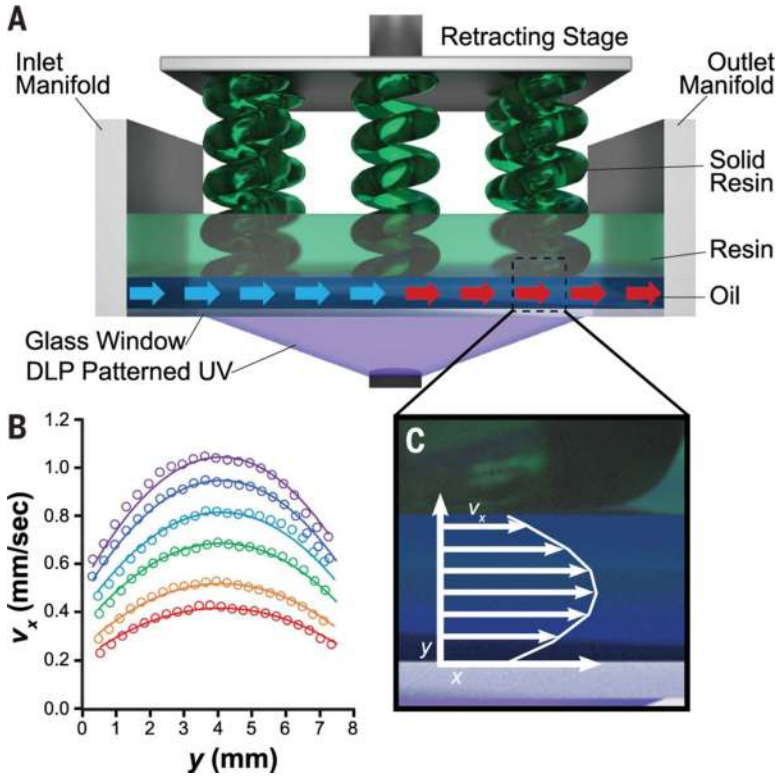

Fig. 1. Flow profile of a mobile interface that enables continuous printing.

(**A**) Scheme of a 3D printed part emerging from the HARP 3D printer. (**B**) Velocity profile under printed part at different flow speeds, demonstrating the presence of a slip boundary. Colors represent increasing volumetric fluxes q (red, $q = 0.21$ mm/s; orange, $q = 0.30$ mm/s; green, $q = 0.44$ mm/s; teal, $q = 0.56$ mm/s; blue, $q = 0.66$ mm/s; violet, $q = 0.75$ mm/s). Open circles are experimental data points from particle-imaging velocimetry; continuous lines are fits from an analytical model. (**C**) Scheme inset of the slip boundary flow profile under the part, with a representative experimentally observed flow profile.

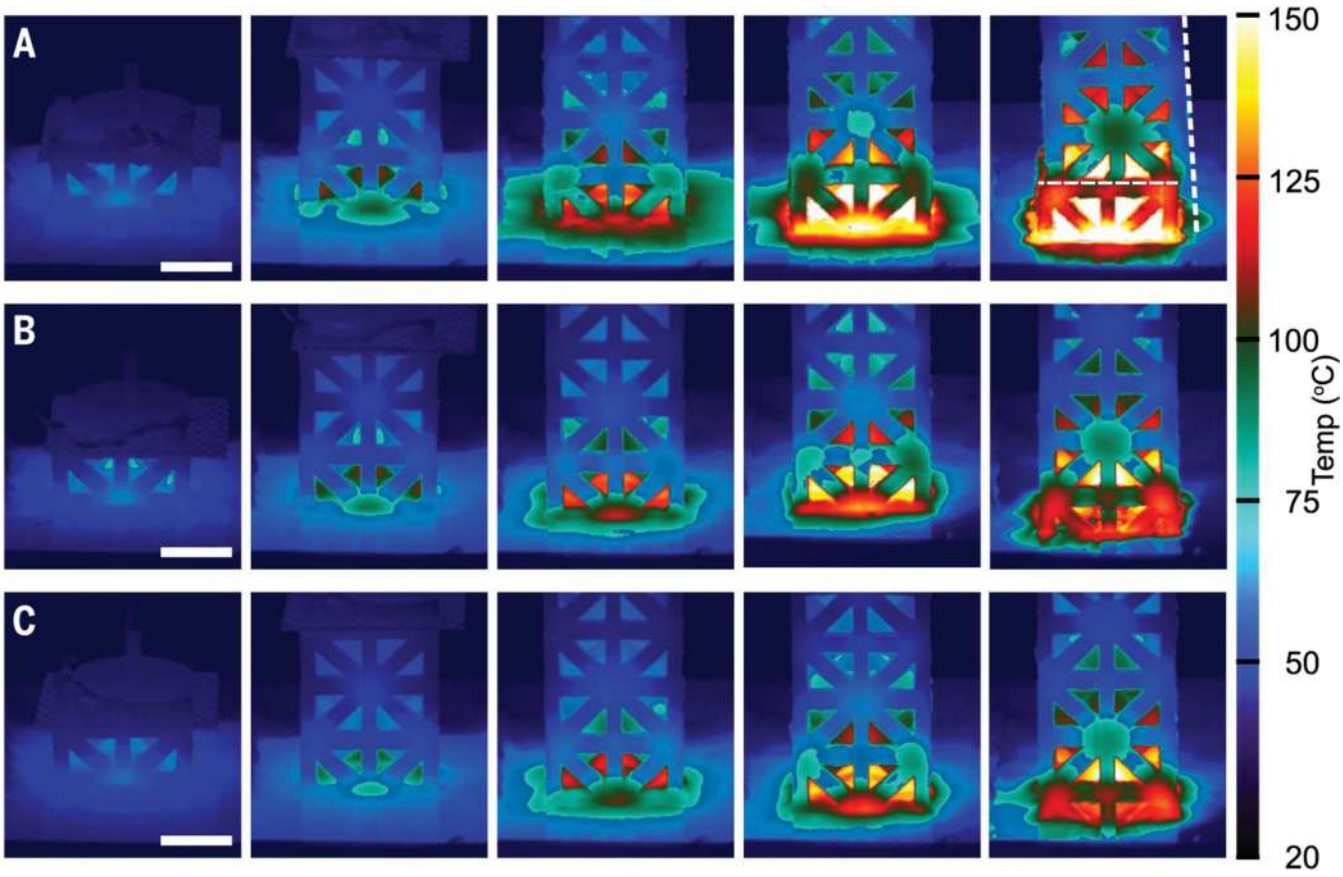

Fig. 2. IR thermal images of an emerging 3D printed part (hard polyurethane acrylate resin; cross section, 5 cm × 5 cm; vertical print rate, 120 μm/s; optical resolution, 100 μm) under three different print conditions.

(**A**) Stationary print interface. (**B**) Mobile interface. (**C**) Mobile interface with active cooling. Elapsed time between panels (left to right) is ~500 s; scale bars, 25 mm. Data and thermal color mapping correspond to movies S1 to S3.

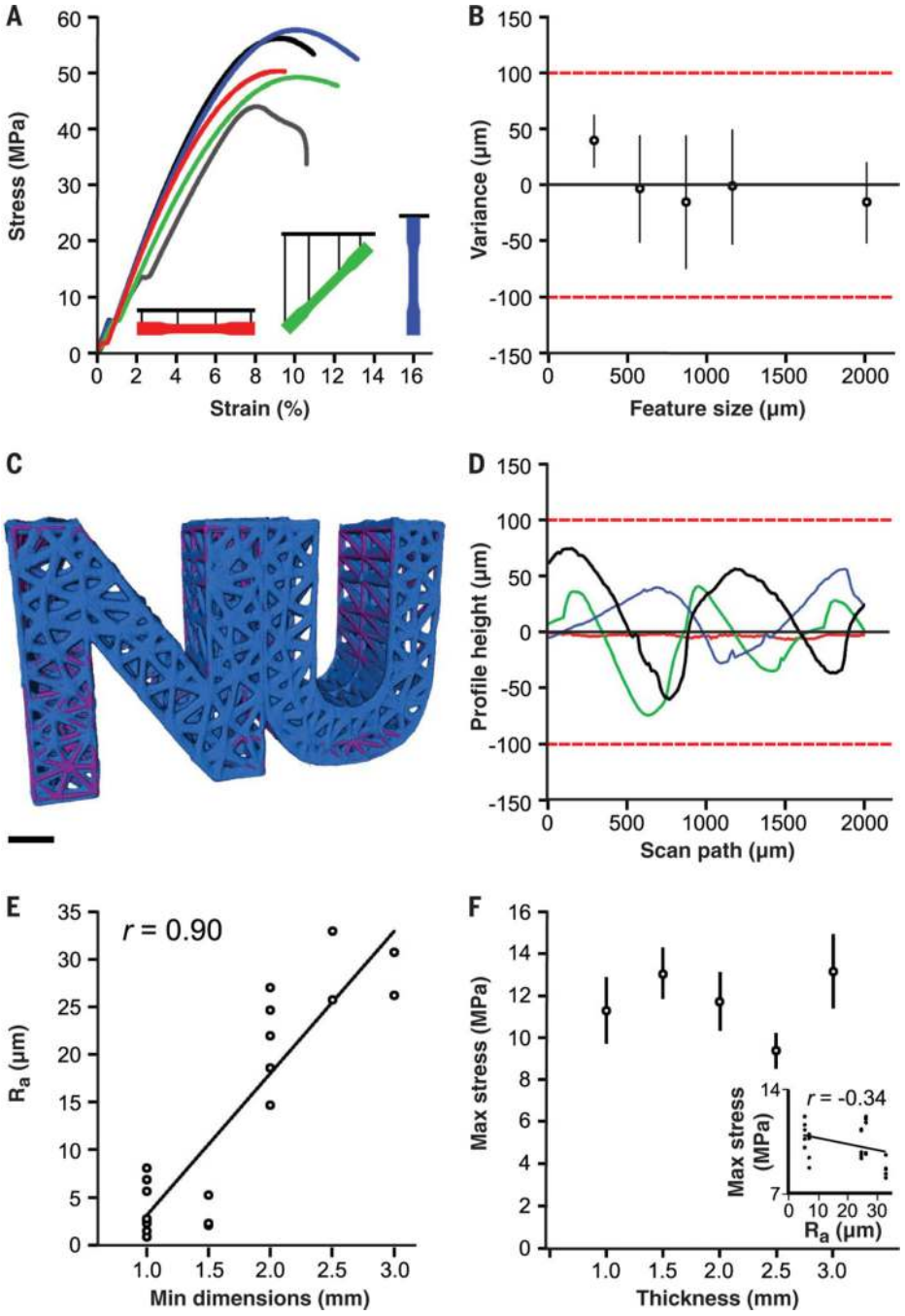

Fig. 3. Manufacturing-ready materials and resolution.

(**A**) Type I dog-bone structures made from an ABS-like polyurethane acrylate resin exhibit isotropic mechanical properties (ASTM D638) and are comparable to a part cast from the same resin (black line) as well as injection molded ABS (gray line). (**B**) HARP also enables high spatial resolution and print fidelity, as evidenced by the variation between designed and printed features as a function of feature size down to ~300 μm (below this, the ability to resolve parts becomes inconsistent) using a light-patterning engine with an optical resolution of 100 μm. Data points are mean values; error bars represent SD across 10 5-mm posts

printed in differing regions of the print bed. Red dashed lines represent the bounding constraints of ±1 pixel for the light-patterning engine. (**C**) A computed tomography (CT) scan between a printed part (print rate, 120 μm/s; optical resolution, 100 μm) and its CAD design file reveals a volumetric correlation of 93%. Blue and purple volumes represent the printed object and the CAD object, respectively. Scale bar, 1 cm. (**D**) Representative height profile scans along the print direction for a series of 3-mm-thick dog bones for varying widths [red, 1 mm; green, 2 mm; blue, 4 mm; black, 6 mm; see additional data in (24) for dog bones 1 to 2.5 mm thick]. Red dashed lines represent the bounding constraints of ±1 pixel for the light-patterning engine. (**E**) Analysis of the profilometry data allows for the calculation of the arithmetic surface roughness, R_a, of the printed parts as a function of minimum feature dimension and reveals a strong linear correlation with a Pearson correlation coefficient of $r = 0.90$ (n = 20, $r_{crit} = 0.444$ for $P = 0.05$). (**F**) Despite this surface roughness, the maximum tensile stress remains invariant of the feature size (data points are mean values; error bars represent SD across five Type IV dog bones, ASTM D638). The inset shows a scatterplot for each dog bone, revealing a Pearson correlation coefficient between the surface roughness and maximum tensile stress of $r = -0.34$ (n = 25, $r_{crit} = 0.396$ for $P = 0.05$). The hard polyurethane acrylate resin was used for all experiments in (B) to (F).

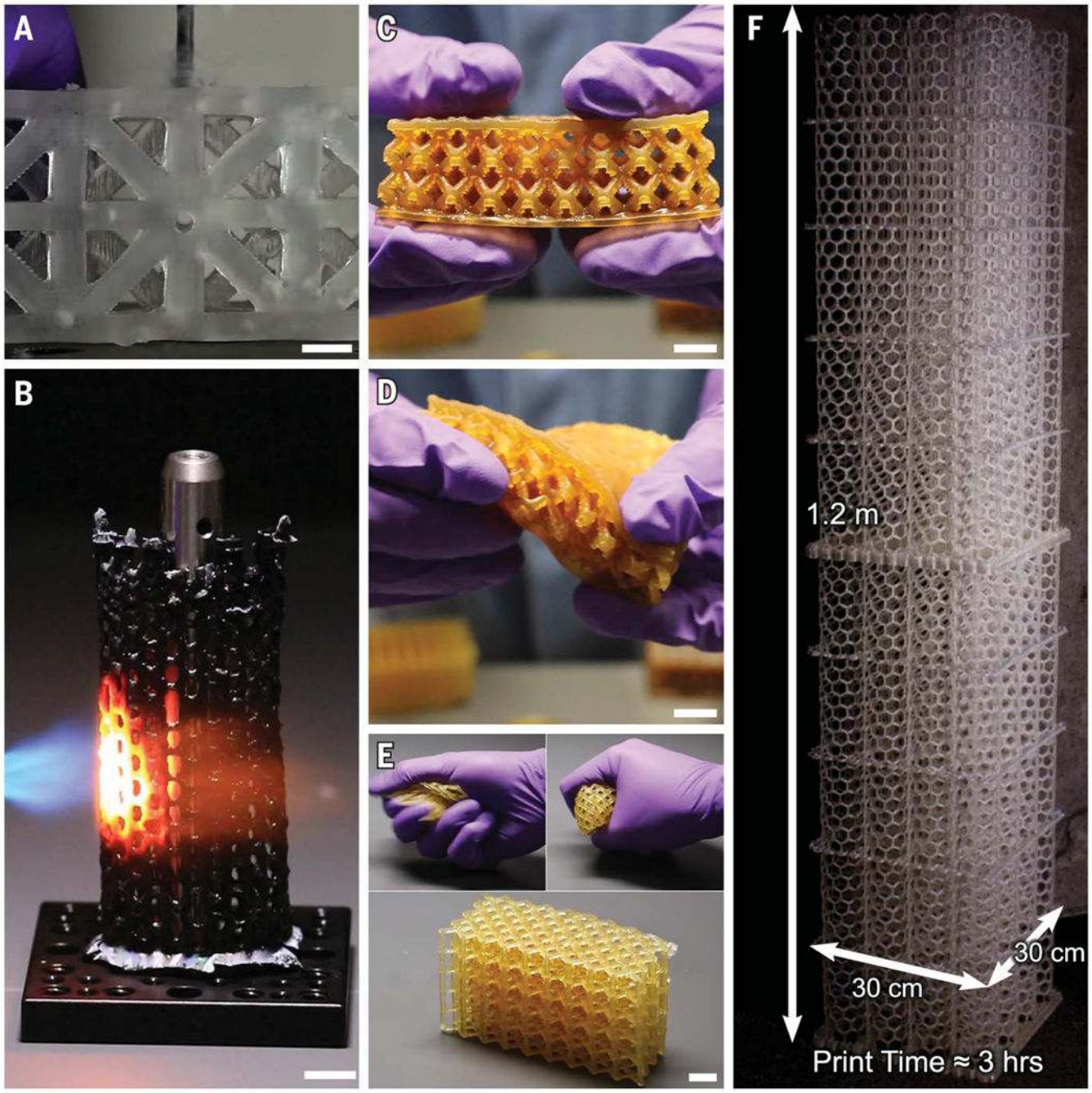

Fig. 4. A wider palette of resins.

(**A**) A hard, machinable polyurethane acrylate part (print rate, 120 μm/s; optical resolution, 100 μm) with a hole drilled against the print direction. Traditional noncontinuous layer-by-layer printing techniques typically delaminate and fracture when drilled in this orientation. (**B**) A post-treated silicon carbide ceramic printed lattice (print rate of green polymer precursor, 120 μm/s; optical resolution, 100 mm) stands up to a propane torch (~2000°C). (**C** and **D**) A printed butadiene rubber structure (print rate, 30 μm/s; optical resolution, 100 μm) in a relaxed state (C) and under tension (D). (**E**) Polybutadiene rubber (print rate, 30 μm/s;

optical resolution, 100 μm) returns to expanded lattice after compression. (**F**) A ~1.2-m hard polyurethane acrylate lattice printed in less than 3 hours (vertical print rate, 120 μm/s; optical resolution, 250 μm). Scale bars, 1 cm.